Design and process test of a novel MOEMS accelerometer based on Raman–Nath diffraction

Zhang Zuwei(张祖伟)[1,2,3,†], Wen Zhiyu(温志渝)[1,2,3], Shang Zhengguo(尚正国)[1,2,3], Li Dongling(李东玲)[1,2,3], and Hu Jing(胡晶)[1,2,3]

[1]Key Laboratory of Fundamental Science on Micro/Nano-Device and System Technology, Chongqing University, Chongqing 400030, China
[2]National Center for International Research of Micro/Nano-System and New Material Technology, Chongqing University, Chongqing 400030, China
[3]Microsystem Research Center of Chongqing University, Chongqing 400030, China

Abstract: A novel micro-opto-electro-mechanical system (MOEMS) accelerometer based on Raman–Nath diffraction is presented. It mainly consists of an FPW delay line oscillator and optical strip waveguides. The fundamental theories and principles of the device are introduced briefly. A flexural plate-wave delay-line oscillator is designed to work as an acousto-optic (AO) shifter, which has a Klein–Cook parameter of 0.38. Single-mode optical strip waveguides of 2 μm in width and thicknesses of 0.6 μm are designed by using the effective index method for light transmission. The E_{00}^{y} mode waveguide polarizers are designed to ensure the consistency of the light polarization in the waveguides. The fabrication process, based on (100) oriented, 450-μm-thick silicon wafers is proposed in detail, and some difficulties in the process are discussed carefully. At last, a series of process tests are undertaken to solve the proposed problems. The results indicate that the proposed design and fabrication process of the device is dependable and realizable.

Key words: accelerometer; MOEMS; Raman–Nath diffraction; design; process test
DOI: 10.1088/1674-4926/33/9/094009 **EEACC:** 2570

1. Introduction

Even though being one of the most successful micro-electro-mechanical system (MEMS) devices and one of the first MEMS devices to be mass-produced, MEMS silicon (Si) accelerometers remain a hot research topic. Typical MEMS Si accelerometers are mainly based on capacitance variation[1,2], piezoresistive effect[3,4], resonant variation[5,6], tunneling effect[7,8], and thermal effect[9,10]. They have advantages of small size, easy integration, and low cost. However most of MEMS Si accelerometers suffer from electromagnetic field interference and require a complex electrical readout, which has to be placed as close as possible to the measuring region.

Micro-opto-electro-mechanical system (MOEMS) accelerometers have attracted increasing attention during the past few years. The combination of a micro-machined Si structure and integrated optics provides several outstanding properties[11]. Firstly, the immunity of integrated optics systems to electromagnetic interference enables them to be placed where a strong electromagnetic field is applied. Secondly, the property of remote sensing allows the light source and photoelectrical detector to be positioned far away from the measured region. Finally, integrated optics circuits never have the possibility of shortcuts or spikes, which may induce dangerous effects in MEMS Si accelerometers. State-of-the-art MOEMS accelerometers can be mainly classified as intensity based[11–13], wavelength encoded[14,15], and interferometric modulated[16–19]. Intensity-based MOEMS accelerometers are easy to set up, reliable, and low cost, but they have the drawback of sensitivity to external disturbance. Wavelength-encoded MOEMS accelerometers usually use a fiber Bragg grating (FBG) as the wavelength modulator. They are not directly affected by external optical intensity change, but they demand a complex signal demodulation system. Interferometer-based MOEMS accelerometers are mainly based on Mach–Zehnder, Michelson, and Fabry–Perot configuration, and they provide the highest sensitivity in vibration sensing.

In this paper, a novel MOEMS accelerometer based on Raman–Nath diffraction is presented. Its operational principle is quite different from the reported MOEMS accelerometers. The device will be fabricated by MEMS technology and consists of a flexural plate-wave (FPW) delay-line oscillator and optical strip waveguides. The FPW delay-line oscillator works as an acousto-optic frequency shifter (AO shifter). When the light propagating in the optical strip waveguides passes through an AO shifter, the Raman–Nath diffraction takes place. The frequency difference between different orders of diffraction light beams is utilized to estimate the change of external acceleration. The principle of the novel accelerometer has been discussed in detail and demonstrated in another paper, which has been published in the *Journal of Semiconductors*[20]. So only a brief description of the principle is presented here. The main motivation of this paper is to demonstrate the possibility of its construction. Therefore the designs of the FPW delay-line oscillator and the optical strip waveguides are discussed in detail, and the fabrication processes are also presented. Furthermore, some process tests are undertaken to demonstrate the feasibility

† Corresponding author. Email: zhangzuwei00@163.com
Received 26 December 2011, revised manuscript received 11 February 2012

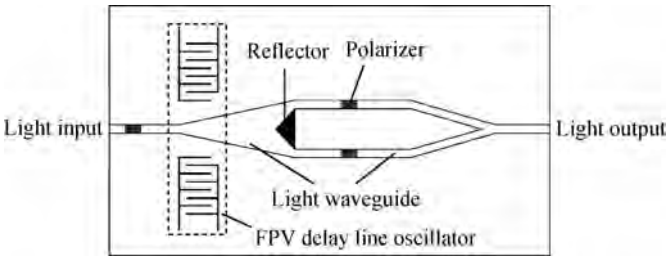

Fig. 1. Schematic of the accelerometer.

of the design.

2. Principle

The novel accelerometer mainly consists of an FPW delay-line oscillator and optical strip waveguides, the schematic diagram is shown in Fig. 1. When the FPW delay-line oscillator produces an acoustic wave propagating in a medium, the stress creates an optical index periodic variation. The variation functions as a diffraction grating and the FPW delay-line oscillator works as an AO shifter. The Raman–Nath diffraction takes place when the light beam in the waveguide passes through the acoustic field if the Klein–Cook parameter of the AO shifter is design too much smaller than 1.

When the AO shifter works at a frequency of f_{a}, the frequency of the $+n$th order diffraction light beam will increase by nf_{a}, while the $-n$th order diffraction light beam will decrease by nf_{a}. If the $+n$th and $-n$th diffraction light beams are collected and superimposed, an optical beat signal with a frequency of $2nf_{\mathrm{a}}$ will be obtained. The $2nf_{\mathrm{a}}$ optical beat signal can be easily detected and translated to a $2nf_{\mathrm{a}}$ electrical signal by using a photoelectric diode (PD).

The AO shifter is designed to be a thin plate structure. Connected to a proof mass, the plate structure AO shifter is sensitive to the external acceleration, and its frequency varies with it. If the frequency change of the AO shifter caused by acceleration is Δf_{a}, the frequency change of the PD output signal will be $2n\Delta f_{\mathrm{a}}$. The sensitivity of the novel accelerometer is greatly improved.

3. Design of the FPW delay line oscillator

The FPW delay line oscillator is fabricated by MEMS technology and has a multilayered thin plate structure built-in at both ends. Firstly, three layers of silicon dioxide (SiO_2) with different reflection indexes are deposited on the Si wafer to form the optical strip waveguides. Secondly, a piezoelectric layer of zinc oxide (ZnO) of 3 μm in thickness is deposited, and interdigital electrodes (IDT) are positioned on the surface of the ZnO layer to excite the acoustic wave. Finally, the Si is thinned to 20 μm from the back of the wafer, and a bridge structure FPW delay line oscillator is obtained.

The FPW delay line oscillator works as an AO shifter in the Raman–Nath regime. The Klein–Cook parameter Q can be expressed as[21]:

$$Q = \frac{2\pi\lambda l}{\lambda_{\mathrm{a}}^2 n_0}, \tag{1}$$

where λ and λ_{a} are the wavelengths of the incident light and the acoustic wave, respectively, n_0 is the reflection index of the medium, and l is the acoustic aperture or the effective width of the acoustic beam. Raman–Nath diffraction occurs when $Q < 1$. λ is determined as 808 nm by using a semiconductor laser. n_0 is determined as 1.465 by using the SiO_2 waveguide. Considering the insert loss of the FPW delay line oscillator, l should not be too small. λ_{a} will be determined by the IDT period. Finally, the acoustic aperture and the IDT period are designed to be 0.7 mm and 80 μm, respectively. In order to make the IDT electrodes raise an activating sound and cut down the insertion spoilage at the same time, the fine width and interval are both $\lambda_a/4 = 20$ μm. The Klein–Cook parameter Q is calculated as 0.38, which is much smaller than 1, therefore the AO shifter will work in the Raman–Nath regime.

The operating frequency of the FPW delay line oscillator can be given by[22]:

$$f_{\mathrm{a}} = \frac{1}{2\pi}\sqrt{\frac{1}{M}\left[D\left(\frac{2\pi}{\lambda_a}\right)^4 + T\left(\frac{2\pi}{\lambda_a}\right)^2\right]}, \tag{2}$$

where D is the effective rigidity of the plate, M is the plate mass per length, and T is the tension in the plate length direction, which domains the thermal effect. The plate consists of a Si layer, a SiO_2 layer, and a ZnO layer. So D can be expressed as:

$$D = \sum_i \frac{E_i\left(I_i + S_i Y_i^2\right)}{1-\nu_i^2}, \tag{3}$$

in which,

$$Y_i = y_i - y_M,$$

and

$$y_M = \frac{\sum\limits_i \dfrac{y_i E_i S_i}{1-\nu_i^2}}{\sum\limits_i \dfrac{E_i S_i}{1-\nu_i^2}},$$

where i is the index for a material layer, E is the Young's modulus, S is the layer cross-section area, y is the vertical distance from center of area to an arbitrary reference, ν is the Poisson's ratio, and I is the area moment of inertia for each layer calculated about its center of area. Ignoring the thermal effect, the operating frequency of the FPW delay line oscillator is calculated as 41.1 MHz.

4. Design of the optical strip waveguides

The coupling of different modes in multimode optical waveguide devices will induce the performance deterioration of the device. So single-mode waveguides are applied in most optical waveguide devices. The effective index method is widely and successfully used in designs and simulations of light wave circuits for it can convert original three-dimension channel waveguides into effective two-dimension planar waveguides. The optical strip waveguides presented in this paper are step-index symmetry embedding single-mode strip waveguides, as shown in Fig. 2(a). Utilizing the effective index method, the optical strip waveguides can be considered as the

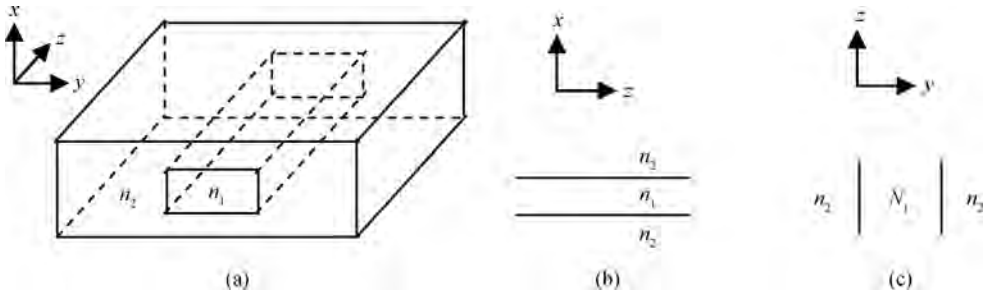

Fig. 2. Schematic of the step-index single-mode embedding strip waveguide.

superimposition of two planar waveguides, which are shown in Figs. 2(b) and 2(c), respectively. The planar waveguide in Fig. 2(b) consists of a core layer with a refraction index of n_1, a substrate with a refraction index of n_2, and a cover layer with a refraction index of n_2. Its effective index is considered as N_1. While the planar waveguide in Fig. 2(c) is proposed to consist of a core layer with a refraction index of N_1, a substrate with the refraction index of n_2, and a cover layer with a refraction index of n_2.

Only the E^y_{mn} mode is discussed here, because the processing of E^x_{mn} mode is totally the same. In the planar waveguide in Fig. 2(b), the E^y_{mn} mode can be considered as the transverse electrical (TE) mode, and the normalized frequency V_1 and normalized refraction index b_1 is defined as:

$$V_1 = k_0 t\sqrt{n_1^2 - n_2^2}, \tag{4}$$

$$b_1 = \frac{N_1^2 - n_2^2}{n_1^2 - n_2^2}, \tag{5}$$

where k_0 is the wave number in vacuum, and t is the thickness of the core layer. The dispersion function of the TE mode in the planar waveguide in Fig. 2(b) can be written as[23]:

$$V_1\sqrt{1-b_1} = m\pi + \tan^{-1}\sqrt{\frac{b_1}{1-b_1}} + \tan^{-1}\sqrt{\frac{b_1 + a_{\mathrm{TE}}}{1-b_1}}, \quad m = 0, 1, 2, \cdots, \tag{6}$$

where m is the mode number, the asymmetry parameter $a_{\mathrm{TE}} = 0$ for symmetry embedding waveguide, and the guided mode cutoff condition is $b_1 = 0$.

In the planar waveguide in Fig. 2(c), the E^y_{mn} mode can be considered as the transverse magnetic (TM) mode, and the normalized frequency V_2 and normalized refraction index b_2 are defined as:

$$V_2 = k_0 w\sqrt{N_1^2 - n_2^2}, \tag{7}$$

$$b_2 = \frac{N^2 - n_2^2}{N_1^2 - n_2^2}, \tag{8}$$

where w is the width of the core layer, N is the effective refraction index of the strip waveguide. The dispersion function of the TM mode in the planar waveguide in Fig. 2(c) can be written as[23]:

$$V_2\left(\frac{\sqrt{\zeta_2}n_1}{n_2}\right)\sqrt{1-b_2} = n\pi + \tan^{-1}\sqrt{\frac{b_2}{1-b_2}} + \tan^{-1}\sqrt{\frac{b_2 + a_{\mathrm{TM}}(1-b_2 d)}{1-b_2}}, \quad n = 0, 1, 2, \cdots, \tag{9}$$

in which n is the mode number, $\zeta_2 = \frac{(n_2/n_1)^2}{1-b_2+b_2(n_2/n_1)^4}$, $d = \left[1 - \left(\frac{n_2}{n_1}\right)^2\right]^2$, asymmetry parameter $a_{\mathrm{TM}} = 0$ for the symmetry embedding waveguide, and the guided mode cutoff condition is $b_2 = 0$.

In order to make sure that the strip waveguide is a single-mode waveguide that transmits only the E^y_{00} mode, firstly the mode of $m = 0$ must propagate while the mode of $m = 1$ must be cutoff in the planar waveguide in Fig. 2(b), then the mode of $n = 0$ must propagate while the mode of $n = 1$ must be cutoff in the planar waveguide in Fig. 2(c). According to Eqs. (6) and (9) and their cutoff conditions, the normalized frequencies V_1 and V_2 can be expressed as:

$$0 < V_1 < \pi, \tag{10}$$

$$0 < V_2 < \pi. \tag{11}$$

Inequation (10) can be transformed into:

$$0 < t < \frac{\lambda}{2\sqrt{n_1^2 - n_2^2}}. \tag{12}$$

Inequation (11) can be transformed into:

$$0 < \frac{w}{t} < \frac{\pi}{V_1\sqrt{b_1}}. \tag{13}$$

The incidence light wavelength $\lambda = 0.808\ \mu$m, SiO_2 core layer refraction index $n_1 = 1.46$, SiO_2 substrate, and cover layer refraction index $n_2 = 1.45$ are applied. The thickness of the strip waveguide core layer is calculated as:

$$0 < t < 2.073\,\mu\mathrm{m}. \tag{14}$$

According to Eq. (6), the relationship between V_1 and b_1 is obtained as shown in Fig. 3(a), consequently the relationship between w/t and t is calculated as shown in Fig. 3(b). The value of w/t seems can be selected to be an arbitrary large one according to Fig. 3(b), but it is usually selected to range from

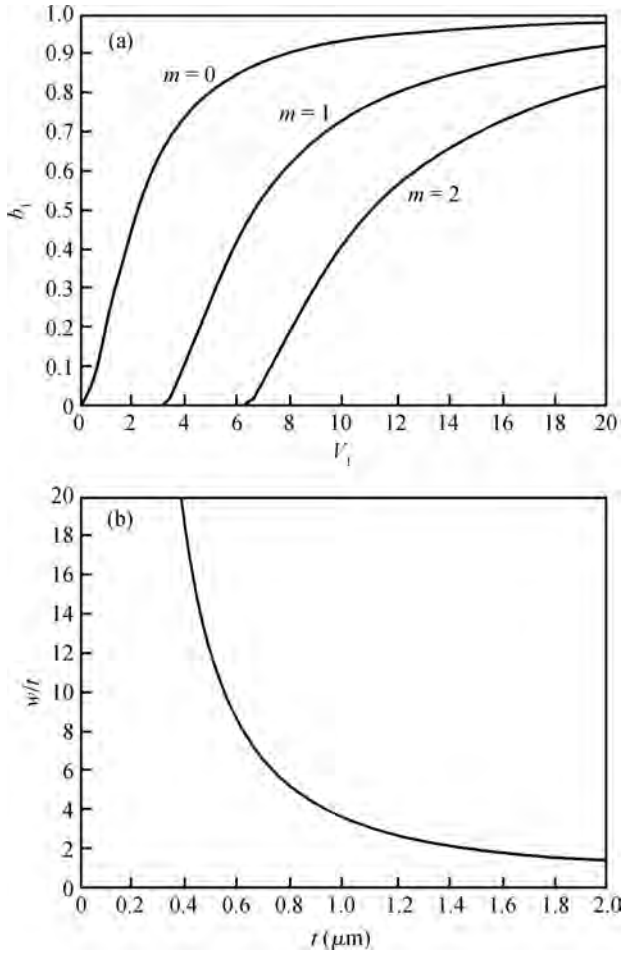

Fig. 3. Relationships between (a) b_1 and V_1 and (b) $\frac{w}{t}$ and t.

1.5 to 2.5 considering the radiation loss caused by bending and the applicable range of the effective index method[23]. In this paper, the SiO_2 core layer, with a thickness of 0.6 μm and a width of 2 μm, is designed to build the optical strip single-mode waveguide.

Through the design of the thickness and width of the waveguide core layer, the higher order modes have been rejected by the cutoff property. However, the cutoff conditions for the fundamental E_{00}^x mode and E_{00}^y mode are very close to each other. If we consider the modulation or the superimposing in integrated optics, the selection of the E_{00}^x mode or the E_{00}^y mode seems to the most important function. Therefore it is necessary to design a polarizer to separate the two fundamental modes. One of the simplest and most useful ways to form a polarizer in an optical strip waveguide is the outer coating of metal film on one side of the optical strip waveguide. It has been reported that the transmission losses of the TM_0 mode is several magnitudes bigger than the TE_0 mode in a planar optic waveguide with an aluminum (Al) film polarizer thicker than 100 nm[24]. That is to say, in optical strip waveguides, Al films of thicknesses of several nanometers coating the upper surface of the waveguides can work as a E_{00}^y mode polarizer. In this paper, an Al film with a thickness of 0.4 μm, width of 2 μm, and length of 400 μm is designed to coat the upper surface of the trip waveguide to form the E_{00}^y mode polarizer.

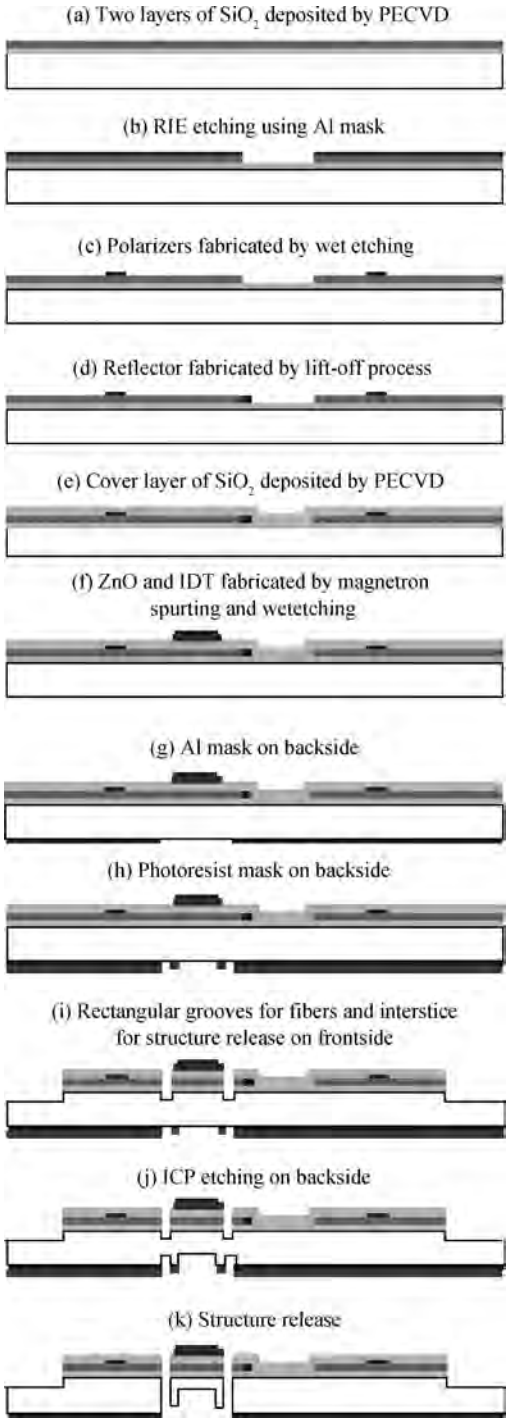

Fig. 4. Fabrication process of the accelerometer.

5. Design of the fabrication process

The accelerometer fabrication process is proposed as shown in Fig. 4. The total process is based on a (100) oriented, 450-μm-thick Si wafer. And it is split into 4 parts for ease of understanding. The first part deals with the fabrication of the optical strip waveguides, including the waveguide polarizers and the waveguide reflector. The second part is the fabrication of ZnO film and IDT. The third part focuses on the dry etching of the rectangular grooves for fixing the optical fibers onto the frontside of the wafer. The last part describes the structural release from the backside of the wafer.

The first part of the process can be separated into seven steps. Firstly, the substrate layer of the optical strip waveguide is obtained by 0.6 μm plasma-enhanced chemical vapor deposition (PECVD) of SiO_2 ($n = 1.455$) on the frontside of the Si wafer. Secondly, another layer of 0.6 μm thick PECVD SiO_2 ($n = 1.465$), the core layer of the waveguide, is deposited on the previous SiO_2 substrate layer, as shown in Fig. 4(a). Thirdly, by utilizing vacuum evaporation and lift-off technology, a 0.4 μm thick Al film is obtained and then patterned to the shape of the optical strip waveguide. The Al pattern has a minimum width of 2 μm and is used as the mask material for the next dry etching. Fourthly, 0.6-μm-deep reactive ion etching (RIE) is applied to pattern the waveguide core layer, as shown in Fig. 4(b). Fifthly, most of the remaining Al pattern is removed by wet etching, except for several certain parts which are used as polarizers, as shown in Fig. 4(c). Sixthly, an Al waveguide reflector is fabricated by using a lift-off process, as shown in Fig. 4(d). The diffraction light beams, which are not expected to be collected, will be reflected by the cross-section of the Al reflector. Seventhly, a layer of 0.7-μm-thick PECVD SiO_2 ($n = 1.45$) is applied to be the cover layer of the optical strip waveguides. The first part of the total process is now complete.

The second part of the process can be separated into two steps. Firstly, a 3-μm-thick ZnO film is obtained by magnetron sputtering and patterned by wet etching. Secondly, a 0.2 μm Cr/Au film is deposited by magnetron sputtering, and IDTs are fabricated on the ZnO patterns by wet etching, as shown in Fig. 4(f).

It is very difficult to remove the photoresist from some structures with a high depth to width ratio, so the masks for backside etching must fabricated before the rectangular grooves and interstices in the third part of the total process are obtained. A 5-μm-thick photoresist is used to cover the topography of the frontside. A 0.5 μm Al film is fabricated by evaporation on the backside and is patterned to open windows for the final structural release by inductively coupled plasma (ICP) etching, as shown in Fig. 4(g). Next, a 5-μm-thick photoresist is applied to cover the backside and patterned as another mask for the forming of the proof mass, as shown in Fig. 4(h). After the two masks on the backside are prepared, 2 μm-deep RIE etching of SiO_2 and 61.5-μm-deep ICP etching of Si on the frontside are used to fabricate the rectangular grooves for optical fiber fixing and the interstices for structural release, as shown in Fig. 4(i). Fibers with a diameter of 125 μm are used to input and output light.

The fourth part of the total process concerns the structural release. It can be separated into to steps. Firstly, a 61.5-μm-deep ICP etching of Si on the backside is applied to format the proof mass, as shown in Fig. 4(j). Then the photoresist mask is removed and ICP etching of Si on the backside is kept on till the bridge structure is released by using the Al mask, as shown in Fig. 4(k). Finally, the fabrication process of the accelerometer is completed.

6. Process test and discussion

There are two main difficulties encountered in the proposed fabrication process. The first one is the fabrication of the optical strip waveguide because of index control, small line width, and the complexity induced by the integration with a polarizer and a reflector. The second one is the accurate control of the dry etching, including RIE and ICP, because no etching stop layer is applied during the whole process. In order to solve these problems, some process tests are presented.

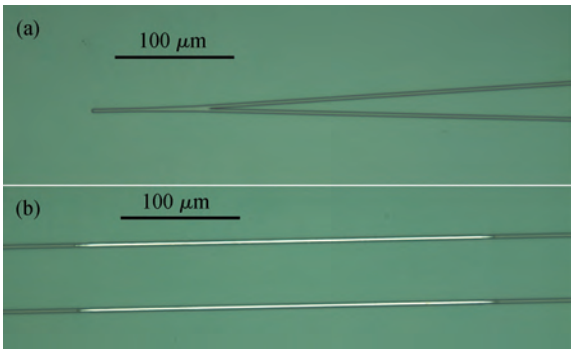

Fig. 5. Morphologies of (a) the optical strip waveguide and (b) the waveguide polarizers.

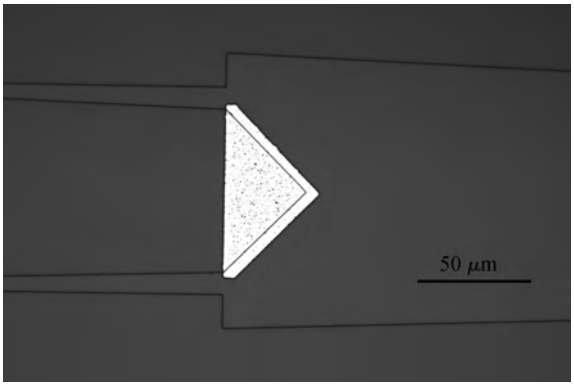

Fig. 6. Morphology of the waveguide reflector.

First of all, SiO_2 films with different refraction indexes must be prepared. SiO_2 film with a refractive index of 1.455 is deposited by using a PECVD process when the temperature is 450 ℃, the pressure is 1 mbar, and the float rate of the silane and the nitrous oxide is 32 sccm/200 sccm. While the float rate of the silane and the nitrous oxide changes to 40 sccm/200 sccm, the SiO_2 film with refractive index of 1.465 is prepared.

The optical strip waveguide is designed to be 2 μm wide. And the polarizer is also a 2 μm wide Al strip film, which is designed to be superposed on the upper surface of the waveguide. It is really hard because the alignment accuracy in a normal photolithographic process is 1–2 μm. So the lift-off process is used to fabricate the waveguide and polarizer, and the morphology is shown in Fig. 5. It can be seen that the boundary of the waveguide is smooth and the Al film superpose on the waveguide perfectly. The single-mode waveguide has a width of 2 μm and a thickness of 0.6 μm.

The waveguide reflector is also fabricated by using lift-off process, as shown in Fig. 6. The fraction light beams come from the right side, which are not expected will be reflected by the mirror formed at the interface between the Al and the SiO_2. While the expected diffraction light beams will be collected into the two strip waveguides.

Table 1. Optimized parameters for the two-step ICP etching process.

Step	Subsycle	SF_6 (sccm)	C_4F_8 (sccm)	O_2 (sccm)	Platen power (W)	Coil power (W)	Etch time (s)	Pressure (mTorr)
One	Etching	150	0	0	22	600	15.5	40
	deposition	0	86	0	0	600	7	20
Two	Etching	150	13	15	20	600	9	40
	deposition	0	85	0	0	600	5	18

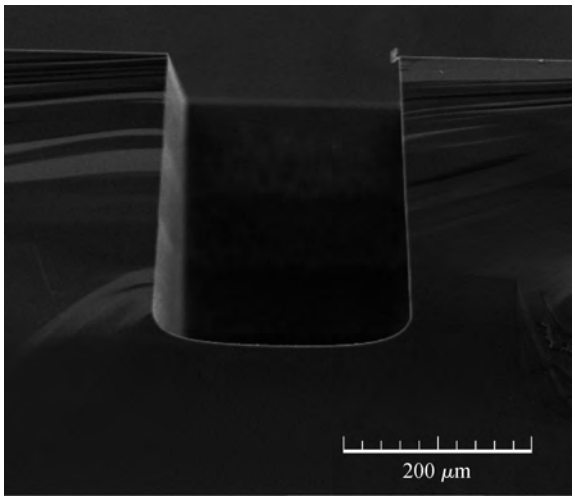

Fig. 7. SEM picture of rectangular groove obtained by the ICP etching.

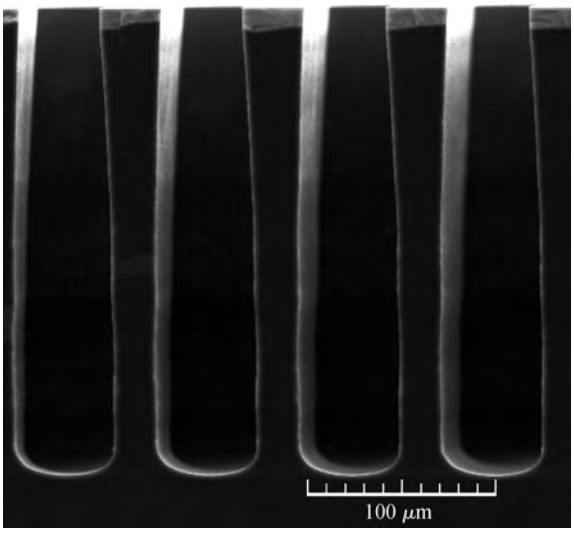

Fig. 8. SEM picture of the high aspect ratio trenches obtained by the ICP etching.

The fabrication of rectangular grooves for optic fiber fixing and the structural release are mainly based on a classic two-step ICP etching process[25] of Si. Two different plasma chemistries are applied in the two-step etching process: the SF_6 gas for etching and the C_4F_8 gas for sidewall passivation. A series of two-step ICP etching methods are employed to explore the control of the etching rate and quality. It is found that the etching rate is mainly determined by the etch/deposition ratio and the discharge power, the quality of the sidewall and bottom depend on the reactive gas flow ratio, except for the chamber temperature and gas flow stability. A group of optimized process parameters is presented in Table 1, and the etching rate is obtained to be about 4 μm/min. Some morphologies of the obtained deep trenches are investigated by using a scanning electron microscope (SEM). The SEM picture of a 200 μm wide, 250 μm deep rectangular groove proposed for optical fiber fixing is shown in Fig. 7. It can be seen that the sidewall and the bottom are both smooth, and the profile angle is almost vertical. These properties are significantly important because of the requirement of collimation between the optical fiber core and the waveguide. The high aspect ratio deep trenches, which can be used for structural release, are also fabricated as shown in Fig. 8. Width of 50 μm, depth of 250 μm, and smooth sidewalls and bottoms are obtained, but a light bow effect is investigated. However, the light bow effect can be ignored because it hardly affects the structural release.

Up to now, several difficulties in the proposed fabrication process have been carefully investigated, and the problems are solved by a series of process tests. The fabrication of the designed single-mode optical strip waveguides is demonstrated to be dependable and realizable.

7. Conclusion

The MOEMS accelerometer is an important MEMS accelerometer research branch with great potential. In this paper, the design and the process test of a novel MOEMS accelerometer based on Raman-Nath diffraction is given. The fundamental theories and principles of the device are introduced briefly. A flexural plate wave delay line oscillator is then designed to work as an acousto-optic (AO) shifter, which has a Klein–Cook parameter of 0.38, an acoustic aperture of 0.7 μm, an IDT period of 80 μm, and an operating frequency of 41.1 MHz. In order to avoid mode coupling induced performance deterioration in the device, single-mode optical strip waveguides with widths of 2 μm and thicknesses of 0.6 μm are designed by using the effective index method. At the same time, E_{00}^{y} mode polarizers made of Al thin film are designed to coat the upper surface of the optical strip waveguides. The fabrication of the device is based on MEMS technology on a (100) oriented, 450 μm thick Si wafer. The total process is proposed in detail, and some difficulties in the process are discussed carefully. Lastly, several process tests are undertaken to solve the proposed difficulties. The result indicates that the proposed design and fabrication process of the device is dependable and realizable.

References

[1] Wen L, Haspeslagh L, De Coster J, et al. Design and characterization of a CMOS compatible poly-SiGe low g capacitive accelerometer. Procedia Engineering, 2010, 5: 742

[2] Sun C, Wang C, Fang W. On the sensitivity improvement of

CMOS capacitive accelerometer. Sensors and Actuators A: Physical, 2008, 141: 347
[3] Kanda K, Iga Y, Matsuoka J, et al. A Tri-axial accelerometer with structure-based voltage operation by using series-connected piezoelectric elements. Procedia Engineering, 2010, 5: 894
[4] Dong P, Li X, Yang H, et al. High-performance monolithic triaxial piezoresistive shock accelerometers. Sensors and Actuators A: Physical, 2008, 141: 339
[5] Pinto D, Mercier D, Kharrat C, et al. A small and high sensitive resonant accelerometer. Procedia Chemistry, 2009, 1: 536
[6] Ferrari V, Ghisla A, Marioli D, et al. Silicon resonant accelerometer with electronic compensation of input-output cross-talk. Sensors and Actuators A: Physical, 2005, 123/124: 258
[7] Dong H, Jia Y, Hao Y, et al. A novel out-of-plane MEMS tunneling accelerometer. Sensors and Actuators A: Physical, 2005, 120: 360
[8] Rockstad H K, Tang T K, Reynolds J K, et al. A miniature, high-sensitivity, electron tunneling accelerometer. Sensors and Actuators A: Physical, 1996, 53: 227
[9] Courteaud J, Crespy N, Combette P, et al. Studies and optimization of the frequency response of a micromachined thermal accelerometer. Sensors and Actuators A: Physical, 2008, 147: 75
[10] Liao K M, Chen R, Chou B C S. A novel thermal-bubble-based micromachined accelerometer. Sensors and Actuators A: Physical, 2006, 130/131: 282
[11] Plaza J A, Llobera A, Dominguez C, et al. BESOI-based integrated optical silicon accelerometer. J Microelectromechan Syst, 2004, 13: 355
[12] De Doncker H W J A, Guan T, Driesen M, et al. Biaxial and uniaxial epoxy accelerometers. Procedia Chemistry, 2009, 1: 572
[13] Cadarso V J, Llobera A, Villanueva G, et al. Polymer microoptoelectromechanical systems accelerometers and variable optical attenuators. Sensors and Actuators A: Physical, 2008, 145/146: 147
[14] Fender A, Macpherson W N, Maier R R J, et al. Two-axis temperature insensitive accelerometer based on multicore fiber Bragg gratings. IEEE Sensors Journal, 2008, 8: 1292
[15] Zhou W, Dong X, Ni K, et al. Temperature-insensitive accelerometer based on a strain-chirped FBG. Sensors and Actuators A: Physical, 2010, 157: 15
[16] Wu B, Chen C, Ding G, et al. Hybrid-integrated Michelson fiber optic accelerometer. Opt Eng, 2004, 43: 313
[17] Perez M, Eklund E J, Shkel A M. Designing micromachined accelerometers with interferometric detection. IEEE Sens, 2005: 652
[18] Ke T, Zhu T, Rao Y, et al. Accelerometer based on all-fiber Fabry–Perot interferometer formed by hollow-core photonic crystal fiber. Microw Opt Technol Lett, 2010, 52: 2531
[19] Gangopadhyay T K. Prospects for fiber Bragg gratings and Fabry–Perot interferometers in fiber-optic vibration sensing. Sens Actuators A: Phys, 2004, 113: 20
[20] Zhang Zuwei, Wen Zhiyu, Hu Jing. Theoretical analysis and concept demonstration of a novel MOEMS accelerometer based on Raman–Nath diffraction. Journal of Semiconductors, 2012, 33(4): 044005
[21] Wu Y, Shankar P M, Lewin P A, et al. Fiber optic ultrasonic sensor using Raman–Nath light diffraction. IEEE Trans Ultrasonics, Ferroelectrics, and Frequency Control, 1994, 41: 166
[22] Weinlerg M S, Cunningham B T, Clapp C W. Modeling flexural plate wave devices. J Microelectromchan Syst, 2000, 9: 370
[23] Fang J X, Cao Z Q, Yang F Z. Physical basis of optic waveguide technology. Shanghai: Shanghai Jiao Tong University Press, 1988
[24] Suematsu Y, Hakuta M, Furuya K, et al. Fundamental transverse electric field (TE_0) mode selection for thin-film asymmetry light guides. Appl Phys Lett, 1972, 21: 291
[25] Bogue R. Developments in advanced silicon etching techniques by STS systems. Sensor Review, 2002, 22: 41